Junzhi Liu, Shantanu Mishra, Carlo A. Pignedoli, Daniele Passerone, José I. Urgel, Alberto Fabrizio, Thorsten G. Lohr, Ji Ma, Hartmut Komber, Martin Baumgarten, Clémence Corminboeuf, Reinhard Berger, Pascal Ruffieux, Klaus Müllen, Roman Fasel, Xinliang Feng

Open-Shell Nonbenzenoid Nanographenes Containing Two Pairs of Pentagonal and Heptagonal Rings

Erstveröffentlichung in / First published in:

Journal of the American Chemical Society. 2019, 141 (30), S. 12011 – 12020. ACS Publications. ISSN 1520-5126.

DOI: https://doi.org/10.1021/jacs.9b04718

JACS
JOURNAL OF THE AMERICAN CHEMICAL SOCIETY
Article
Cite This: J. Am. Chem. Soc. 2019, 141, 12011−12020
pubs.acs.org/JACS

Open-Shell Nonbenzenoid Nanographenes Containing Two Pairs of Pentagonal and Heptagonal Rings

Junzhi Liu,[†,○] Shantanu Mishra,[‡,○] Carlo A. Pignedoli,[‡,§] Daniele Passerone,[‡,§] José I. Urgel,[‡] Alberto Fabrizio,[§,∥] Thorsten G. Lohr,[†] Ji Ma,[†] Hartmut Komber,[⊥] Martin Baumgarten,[#] Clémence Corminboeuf,[§,∥] Reinhard Berger,[†] Pascal Ruffieux,[‡] Klaus Müllen,[*,#] Roman Fasel,[*,‡,▽] and Xinliang Feng[*,†]

[†]Center for Advancing Electronics Dresden (cfaed) & Department of Chemistry and Food Chemistry, Technische Universität Dresden, 01062 Dresden, Germany

[‡]Empa, Swiss Federal Laboratories for Materials Science and Technology, Überlandstrasse 129, 8600 Dübendorf, Switzerland

[§]National Centre for Computational Design and Discovery of Novel Materials (MARVEL), 1015 Lausanne, Switzerland

[∥]Laboratory for Computational Molecular Design, École Polytechnique Fédérale de Lausanne, Avenue F.-A. Forel 2, 1015 Lausanne, Switzerland

[⊥]Leibniz-Institut für Polymerforschung Dresden e.V., Hohestraße 6, 01069 Dresden, Germany

[#]Max-Planck Institut für Polymerforschung, 55128 Mainz, Germany

[▽]Department of Chemistry and Biochemistry, University of Bern, Freiestrasse 3, 3012 Bern, Switzerland

Supporting Information

ABSTRACT: Nonbenzenoid carbocyclic rings are postulated to serve as important structural elements toward tuning the chemical and electronic properties of extended polycyclic aromatic hydrocarbons (PAHs, or namely nanographenes), necessitating a rational and atomically precise synthetic approach toward their fabrication. Here, using a combined bottom-up in-solution and on-surface synthetic approach, we report the synthesis of nonbenzenoid open-shell nanographenes containing two pairs of embedded pentagonal and heptagonal rings. Extensive characterization of the resultant nanographene in solution shows a low optical gap, and an open-shell singlet ground state with a low singlet−triplet gap. Employing ultra-high-resolution scanning tunneling microscopy and spectroscopy, we conduct atomic-scale structural and electronic studies on a cyclopenta-fused derivative on a Au(111) surface. The resultant five to seven rings embedded nanographene displays an extremely narrow energy gap of 0.27 eV and exhibits a pronounced open-shell biradical character close to 1 (y_0 = 0.92). Our experimental results are supported by mean-field and multiconfigurational quantum chemical calculations. Access to large nanographenes with a combination of nonbenzenoid topologies and open-shell character should have wide implications in harnessing new functionalities toward the realization of future organic electronic and spintronic devices.

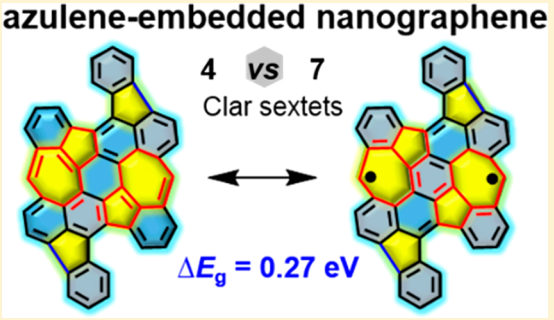

INTRODUCTION

Extended polycyclic aromatic hydrocarbons, or nanographenes, which can be regarded as finite graphene segments composed of sp^2-conjugated carbon atoms, have attracted tremendous interest in the past two decades due to their intriguing electronic and optoelectronic properties, leading to potential applications in organic electronics.[1−3] In this regard, bottom-up synthesis serves as an indispensable tool to furnish structurally well-defined nanographenes, which is essential for reliable structure−property relationships in graphene nanostructures.[4] Fundamental contributions to the bottom-up synthesis of nanographenes date back to Scholl and Clar at the beginning of the 20th century, who obtained numerous nanographenes under drastic conditions including pentacene and hexa-*peri*-hexabenzocoronene.[5−7] Progress in analytical techniques led to remarkable synthetic breakthroughs, which made it possible to selectively synthesize various nanographenes under relatively mild conditions.[2] In the past two decades, these bottom-up organic synthesis approaches have afforded a wide variety of nanographenes with different molecular sizes, shapes, symmetries, and edge topologies.[3] Of particular relevance are advances in the synthesis of structurally defined graphene nanoribbons as new-generation semiconductors.[8−14] However, most reported nanographenes consist solely of benzenoid rings. Nonbenzenoid odd-membered polycycles

Received: May 4, 2019
Published: July 12, 2019

DOI: 10.1021/jacs.9b04718
J. Am. Chem. Soc. 2019, 141, 12011−12020

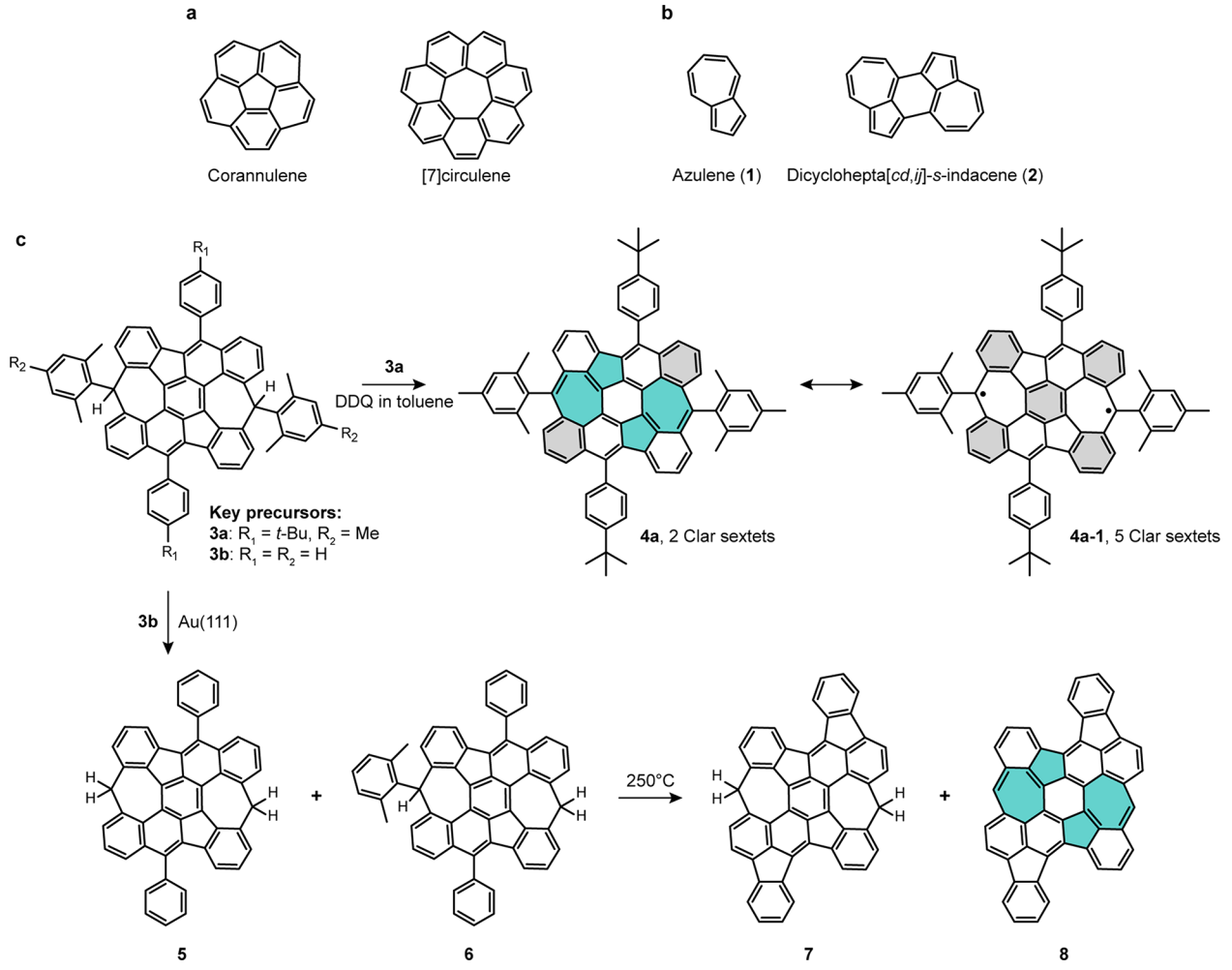

Figure 1. In-solution and on-surface synthetic routes toward azulene-embedded nanographenes **4a** and **8**. (a) Representative PAHs containing pentagonal or heptagonal rings. (b) Nonbenzenoid building blocks of the structures reported in this study. (c) Synthetic routes toward the nanographenes containing two pairs of embedded pentagonal and heptagonal rings, based on the key precursor **3**. Blue filled rings highlight pentagonal and heptagonal rings. Gray filled rings represent Clar sextets.

such as pentagons and heptagons[15−21] (Figure 1a) occur in graphene as localized defects and extended grain boundaries,[22−27] and may significantly influence the physicochemical properties of corresponding nanostructures, arising from local changes in strain and conjugation.[28−30] The known methods of graphene fabrication, however, fail to offer a rational control over the formation of nonbenzenoid topologies. This limitation thus motivates their atomically precise synthesis and comprehensive characterizations. Concurrently, significant efforts have been devoted toward the synthesis and characterization of open-shell nanographenes containing unpaired electrons.[31−33] The interest in such compounds is driven by their potential application in all-organic spintronic devices.[34] While a growing number of multiple open-shell structures with biradical to polyradical characters have been recently achieved, most of them exhibited an all-benzenoid topologies.[35] Consequently, open-shell nanographenes with nonbenzenoid topologies have remained elusive.[36−38]

Herein, we report on a combined in-solution and on-surface synthesis of a new family of nonbenzenoid nonalternant open-shell nanographenes containing a fully conjugated aromatic core with two pairs of embedded pentagonal and heptagonal rings (**1**, Figure 1b), namely dicyclohepta[*cd*,*ij*]-*s*-indacene (**2**, Figure 1b). Based on the key precursor **3a**, its oxidation in solution yields the azulene-embedded polycyclic aromatic hydrocarbon (PAH) **4a** (Figure 1c). Compound **4a** exhibits a narrow optical energy gap of 1.13 eV and an open-shell singlet ground state as indicated by electron paramagnetic resonance (EPR), variable-temperature nuclear magnetic resonance (VT-NMR), and superconducting quantum interference device (SQUID) studies. To apply this synthetic strategy on a surface, precursor **3b** without peripheral methyl and *tert*-butyl groups was synthesized. After deposition of **3b** on a Au(111) substrate and annealing to 250 °C under ultrahigh vacuum (UHV) conditions, a mixture of different products was obtained. Importantly, successful on-surface synthesis of a cyclopenta-fused azulene-embedded PAH **8** (Figure 1c) was achieved. Employing bond-resolved scanning tunneling microscopy (STM) at low temperatures (T = 5 K), we unambiguously elucidated the chemical structure of **8**. Through scanning tunneling spectroscopy (STS) measurements, we unravel an ultralow highest occupied molecular orbital (HOMO)−lowest unoccupied molecular orbital (LUMO) gap of 0.27 eV of **8** on Au(111), and image the spatial distributions of the probability densities of the corresponding frontier orbital wave functions. Our results are supported by density functional theory (DFT), unrestricted Hartree−Fock (UHF), and general multiconfigurational quasi-

DOI: 10.1021/jacs.9b04718
J. Am. Chem. Soc. 2019, 141, 12011−12020

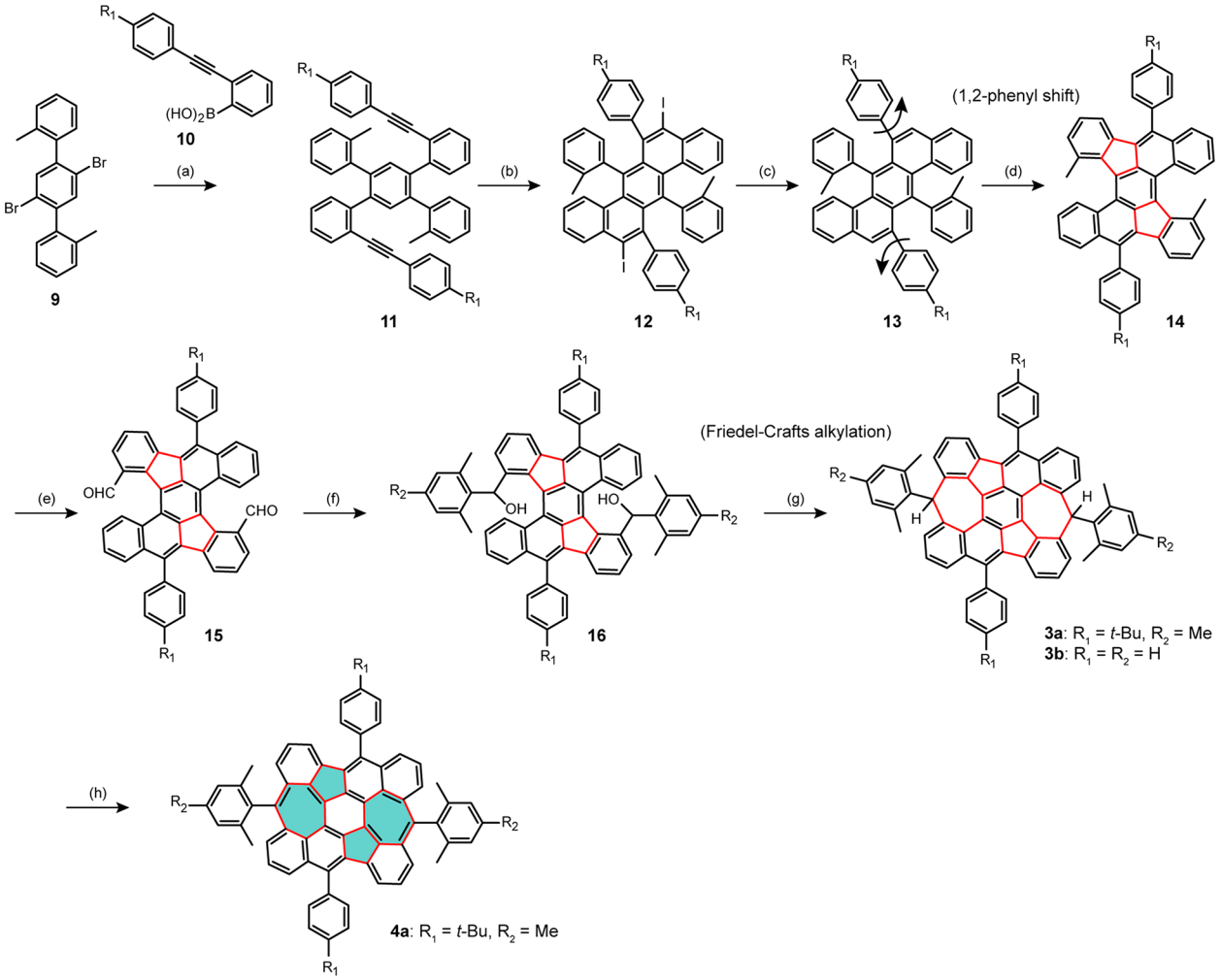

Figure 2. Total synthetic route toward **4a**. Reagents and conditions: (a) $Pd(PPh_3)_4/K_2CO_3$, dioxane/H_2O, 90 °C, 24 h, **11a**: 75%, **11b**: 69%. (b) ICl (1 M in DCM), DCM, −78 °C, 3 h, **12a**: 85%, **12b**: 71%. (c) *n*-BuLi, THF, −78 °C, 1 h, **13a**: 53%, **13b**: 50%. (d) DDQ/CF_3SO_3H, DCM, 0 °C, 1 h, **14a**: 65%, **14b**: 45%. (e) (1) NBS, BPO, CCl_4, reflux; (2) KOAc, Bu_4NBr, DMF, 100 °C; (3) KOH(aq), THF/EtOH, reflux; (4) PCC, DCM, room temperature, **15a**: 32%, **15b**: 28% in four steps. (f) Mesitylmagnesium bromide, THF, room temperature. (g) $BF_3{\cdot}OEt_2$, DCM, room temperature, **3a**: 58%, **3b**: 40% yield in two steps. (h) DDQ, toluene, 80 °C, 2 h, **4a**: 25%. NBS, *N*-bromosuccinimide; BPO, benzoyl peroxide; Bu_4NBr, tetra-*n*-butylammonium bromide; PCC, pyridinium chlorochromate; DDQ, 2,3-dichloro-5,6-dicyano-1,4-benzoquinone. Nonbenzenoid rings formed during the reactions are highlighted in red. Blue filled rings highlight azulene units.

degenerate perturbation theory (GMC-QDPT2) calculations. The azulene-embedded nanographenes reported herein open avenues toward fabrication of novel nonbenzenoid nonalternant graphene nanostructures.

RESULTS

In-Solution Synthesis of Precursors 3a and 3b, and the Azulene-Embedded Nanographene 4a. Synthesis of the target compounds **3** and **4** is described in Figure 2. Selective Suzuki coupling between 1,4-dibromo-2,5-diiodobenzene and commercially available *o*-tolylboronic acid provided 2′,5′-dibromo-2,2″-dimethyl-1,1′:4′,1″-terphenyl (**9**) in 80% yield. Then compound 2-((4-(*tert*-butyl)phenyl)ethynyl)-4′-(2-((4-(*tert*-butyl)phenyl)ethynyl)phenyl)-2″-methyl-5′-(*o*-tolyl)-1,1′:2′,1″-terphenyl (**11a**) was obtained by Suzuki coupling of **9** with (2-((4-(*tert*-butyl)phenyl)ethynyl)phenyl)-boronic acid (**10**) in 75% yield. Afterward, utilizing ICl-induced cyclization of **11a** afforded compound 6,13-bis(4-(*tert*-butyl)phenyl)-5,12-diiodo-7,14-di-*o*-tolylbenzo[*k*]tetraphene (**12a**) in 85% yield. Removing the iodine groups of **12a** by *n*-BuLi furnished 6,13-bis(4-(*tert*-butyl)phenyl)-7,14-di-*o*-tolylbenzo[*k*]tetraphene (**13a**) in 53% yield. The cyclodehydrogenation of **13a** was performed with 2,3-dichloro-5,6-dicyano-1,4-benzoquinone (DDQ)/trifluoromethanesulfonic acid (CF_3SO_3H) as the Lewis oxidant/acid in dry dichloromethane (DCM) at 0 °C under argon, leading to 5,14-bis(4-(*tert*-butyl)phenyl)-9,18-dimethyldibenzo[*a*,*m*]rubicene (**14a**) as reddish-brown powder in 65% yield. Subsequently, the dimethyl groups of **14a** were transformed into dialdehyde functions to provide 5,14-bis(4-(*tert*-butyl)phenyl)dibenzo-[*a*,*m*]rubicene-9,18-dicarbaldehyde (**15a**) via a bromination−esterification−hydrolysis−oxidation sequence in a yield of 32% in four steps. Single crystals of **15a** were carefully grown by slow evaporation from solution in DCM/hexane, and the structure of **15a** was elucidated via X-ray diffraction (Figure 3a). Compound **15a** was treated with mesitylmagnesium bromide to give diol **16a**, which was subjected to Friedel−Crafts alkylation promoted by $BF_3{\cdot}OEt_2$ to afford 4,12-bis(4-(*tert*-butyl)phenyl)-8,16-dimesityl-8,16-dihydropleiadeno-[2′,1′,12′,11′:3,4,5,6]-*s*-indaceno[2,1,8,7-*nopqa*]pleiadene (**3a**)

DOI: 10.1021/jacs.9b04718
J. Am. Chem. Soc. 2019, 141, 12011−12020

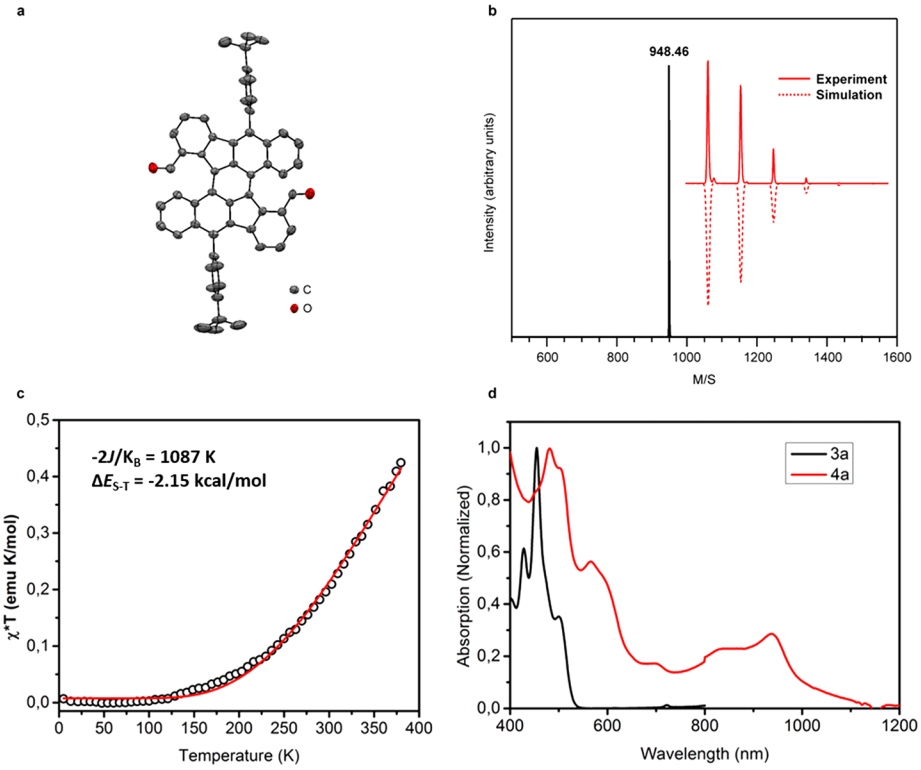

Figure 3. Structural analysis of **15a** and spectroscopic analyses of **3a** and **4a**. a Top view of the X-ray crystallographic structure (ORTEP drawing) of **15a**. Hydrogen atoms and solvent molecules are omitted for clarity. (b) HR-MALDI-TOF mass spectrum of **4a**. Inset: experimental (red solid line) and simulated (red dashed line) isotopic distribution patterns of the mass peak. (c) Experimental χ^*T-T curve of a powder sample of **4a** measured via SQUID (black circles). The red curve is a fit to the experimental data with the Bleaney–Bowers equation with $g_e = 2$. (d) Normalized UV–vis absorption spectra of **3a** and **4a** in a 1×10^{-5} M DCM solution.

in 58% yield in two steps. Following a similar synthetic strategy, compound **3b** without the *tert*-butyl groups was obtained, which served as the precursor for surface-assisted dehydrogenation. In solution, oxidation of **3a** with DDQ in dry toluene at 80 °C under argon produced the target compound **4a** as a purple powder in 25% yield. To confirm the formation of **4a**, the solution of **4a** in dry DCM was examined with the aid of high-resolution matrix-assisted laser desorption/ionization time-of-flight (HR-MALDI-TOF) mass spectrometry, as shown in Figure 3b. There is only one dominant peak in the mass spectrum of **4a**, revealing its well-defined molecular composition. The isotopic distribution pattern of the mass peak is in good agreement with the calculated one.

In-Solution Characterization of 4a. To gain insights into the physicochemical properties of **4a**, VT-^{1}H NMR experiment of **4a** from 30 to −80 °C in toluene-d_8 was performed (Figure S1 of the Supporting Information). Whereas no aromatic signals were observed above −70 °C, a very broad signal appeared in the aromatic protons region as the temperature was cooled below −70 °C. When the sample temperature was increased back to 30 °C, this signal disappeared again. These results indicated that a thermally accessible triplet state was populated, resulting in NMR signal broadening. Upon decreasing the temperature, the population of the triplet state decreased, and the aromatic protons signal could be observed as a very broad but detectable signal. From the resonance structures drawn in Figure 1c, there are two aromatic sextets (the hexagons highlighted in gray color) in the closed-shell form of **4a** and a maximum of five aromatic sextets in the non-Kekulé biradical form **4a-1**. Theoretical and experimental results have demonstrated that the major driving force for a singlet biradical ground state is the gain of additional Clar sextet rings in the biradical resonance form in comparison to the closed-shell resonance form, as a result of gaining the aromatic stabilization energies.[35,39]

To further investigate the open-shell character of **4a**, EPR measurements were carried out both in the solution and in the solid state. Compound **4a** in toluene at room temperature yielded a well-resolved EPR spectrum with five lines (Figure S2), which can be well-reproduced by spectral simulation with two sets of two larger proton hyperfine couplings ($2a_{H1}$ = 4.20 G, $2a_{H2}$ = 4.00 G) giving rise to five main lines and two smaller proton couplings ($2a_{H3}$ = 0.70 G) resulting in another split of each of the five lines in a triplet. Notably, the biradical feature in frozen toluene solution could only be identified in the narrow temperature range of 160–190 K, where the matrix softened already and completely lost below 150 K (Figure S3). A more extended measurement at 180 K yielded clear pronounced zero field splitting components of spacing 2*D* and *D*, where the distance of *D* is approximately 62.8 mT (Figure S4). The freshly prepared **4a** in the solid state gave an unresolved EPR spectrum for a biradical with a broad peak at a *g*-value of 2.003, as a result of both the inter- and intramolecular interactions (Figure S5). Furthermore, upon increasing the temperature, the solid-state EPR signal intensity increased, resulting from a thermally excited triplet state which is slightly higher in energy than the singlet biradical state. Furthermore, SQUID measurements were carried out with the powder sample of **4a**, in the temperature range 5–400 K (Figure 3c). The result showed an increasing molar magnetic

DOI: 10.1021/jacs.9b04718
J. Am. Chem. Soc. 2019, 141, 12011–12020

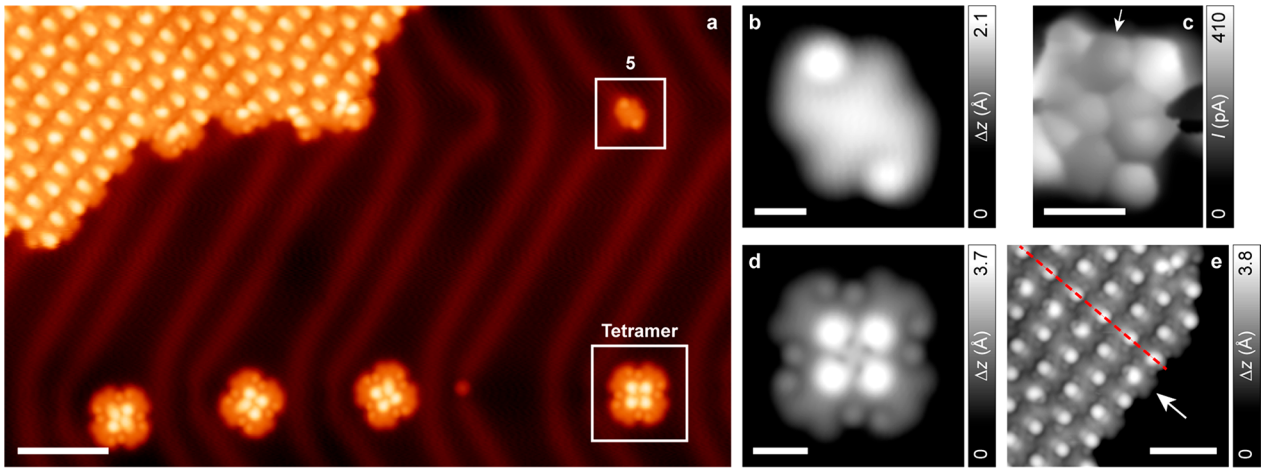

Figure 4. Deposition of precursor **3b** on Au(111). (a) Overview STM topography image of the Au(111) surface after deposition of **3b** (V = −1 V, I = 50 pA; scale bar 5 nm). (b) High-resolution STM image of **5** highlighted in the upper-right corner in panel a (V = −50 mV, I = 50 pA; scale bar 0.5 nm). (c) UHR-STM image of the core of **5** (open feedback parameters: V = −7 mV, I = 50 pA, Δz = −0.5 Å; scale bar 0.5 nm). The arrow indicates a heptagonal ring with a missing xylenyl group. The instability at the boundaries of the scan frame arises due to interaction of the CO tip with the flexible phenyl rings of the molecule. Individual molecules were difficult to image at reduced tip−molecule distances due to their lateral movement. UHR-STM imaging was thus performed on molecules that were found to be noncovalently attached to the tetramers, as such molecules were stable under our imaging conditions. The scan frame in panel c was chosen so as to minimize the interaction of the CO with the phenyl rings of the adjacent molecules of the tetramers, resulting in a cutoff region in the bottom-left part. (d) High-resolution STM image of a self-assembled tetramer of **6** highlighted in the bottom-right corner in panel a (V = −50 mV, I = 50 pA; scale bar 1 nm). (e) High-resolution STM image of a self-assembled island (V = −70 mV, I = 50 pA; scale bar 3 nm). The arrow highlights a single unit of **6** at the periphery, evidencing it as the constituent unit of the island. The red dashed line indicates a row of molecules along which their orientation remains the same.

susceptibility (χ*) above 150 K, and fitting of the data by the Bleaney−Bowers equation yielded a singlet−triplet energy gap (ΔE_{S-T}) of −2.15 kcal/mol. From DFT calculations on **4a** (performed at the UB3LYP level), we obtained ΔE_{S-T} = −1.14 kcal/mol, very close to the value measured by SQUID (ΔE_{S-T} = −2.15 kcal/mol), which further affirmed the open-shell singlet as the ground state. Our extensive characterizations thus confirm that **4a** displays a singlet open-shell ground state.

We also performed UV−vis absorption spectroscopy of precursor **3a** and the dehydrogenated **4a** in a degassed DCM solution (Figure 3d), wherein **3a** was found to show a well-resolved peak at λ = 501 nm. In contrast, the absorption spectrum of **4a** exhibits a broad band in the near-infrared region with a maximum at λ = 936 nm. The optical energy gap (E_g^{opt}) of **4a** was determined to be 1.13 eV based on the lowest energy absorption onset. To investigate the stability of **4a** under ambient condition, we measured the time-dependent absorption spectrum of **4a** in DCM while it was exposed to air. Notably, with increasing time, the solution exhibited increasing absorption in the region between 522 and 649 nm along with a concomitant decrease of the absorption peak intensities in the near-infrared region (Figure S6). A plot of the percentage absorbance change at 936 nm against time showed a gradual decrease, and based on a linear fit of the data, the half-life time of **4a** was estimated to be ∼2 h (Figure S7). Cyclic voltammetry (CV) of **4a** (Figure S8) was performed in a DCM solution containing 0.1 M $TBAPF_6$ (vs Ag/AgCl). One reversible oxidation and one pseudoreversible oxidation occurred at 0.11 (E^1_{ox}) and 0.61 V (E^2_{ox}), respectively, whereas three irreversible oxidations were observed at 0.83 (E^3_{ox}), 1.01 (E^4_{ox}), and 1.34 V (E^5_{ox}), respectively. The CV analysis thus suggests that **4a** is unstable due to its lower oxidation potential. The HOMO energy level was estimated to be −4.51 eV from the onset potential of the first oxidation wave. The LUMO energy level was calculated to be −3.38 eV based on the HOMO level and optical gap (E_g^{opt}=1.13 eV).

On-Surface Synthesis and Characterization of Azulene-Embedded Nanographene 8. Since the in-solution approach suffers from the instability of **4a**, we explored the possibility of surface-assisted dehydrogenation of precursor **3b** (without the presence of bulky methyl and *tert*-butyl substituents) toward the formation of nanographenes with embedded azulene units. After sublimation of **3b** on an atomically clean Au(111) surface held at room temperature, large-scale STM image (Figure 4a) reveals the predominant presence of self-assembled islands and discrete square-shaped units, along with a minor amount of individual molecules. We find that almost all the molecules exhibit complete (**5**) or partial (**6**) loss of xylenyl groups, and intact precursor molecules (i.e., **3b**) are rarely observed on the surface (Figure S9). Figure 4b shows a high-resolution STM image of **5**, which consists of a planar core and two peripheral lobes of 2.1 Å in apparent height. The absence of any prominent feature of large apparent height hints at a complete loss of xylenyl groups attached to the heptagonal rings. However, further structural characterization of **5** is difficult via STM imaging alone, that probes only the local density of states (LDOS) near the Fermi energy and is insensitive to the chemical structure of a molecule. To circumvent this limitation, we functionalize the STM tip with a carbon monoxide (CO) molecule to conduct imaging in the regime of Pauli repulsion.[40,41] Figure 4c shows the ultrahigh resolution (UHR) STM image of the core of **5** acquired with a CO-functionalized tip, which clearly shows the molecular framework and confirms the complete loss of xylenyl groups from the apexes of the heptagonal rings. The radical sites generated from the loss of xylenyl substituents are likely passivated by hydrogen that is present as a residual gas in the UHV chamber, resulting in dihydrogenated apical carbon atoms of the heptagonal rings (Figure 1c). STS measurements

DOI: 10.1021/jacs.9b04718
J. Am. Chem. Soc. 2019, 141, 12011−12020

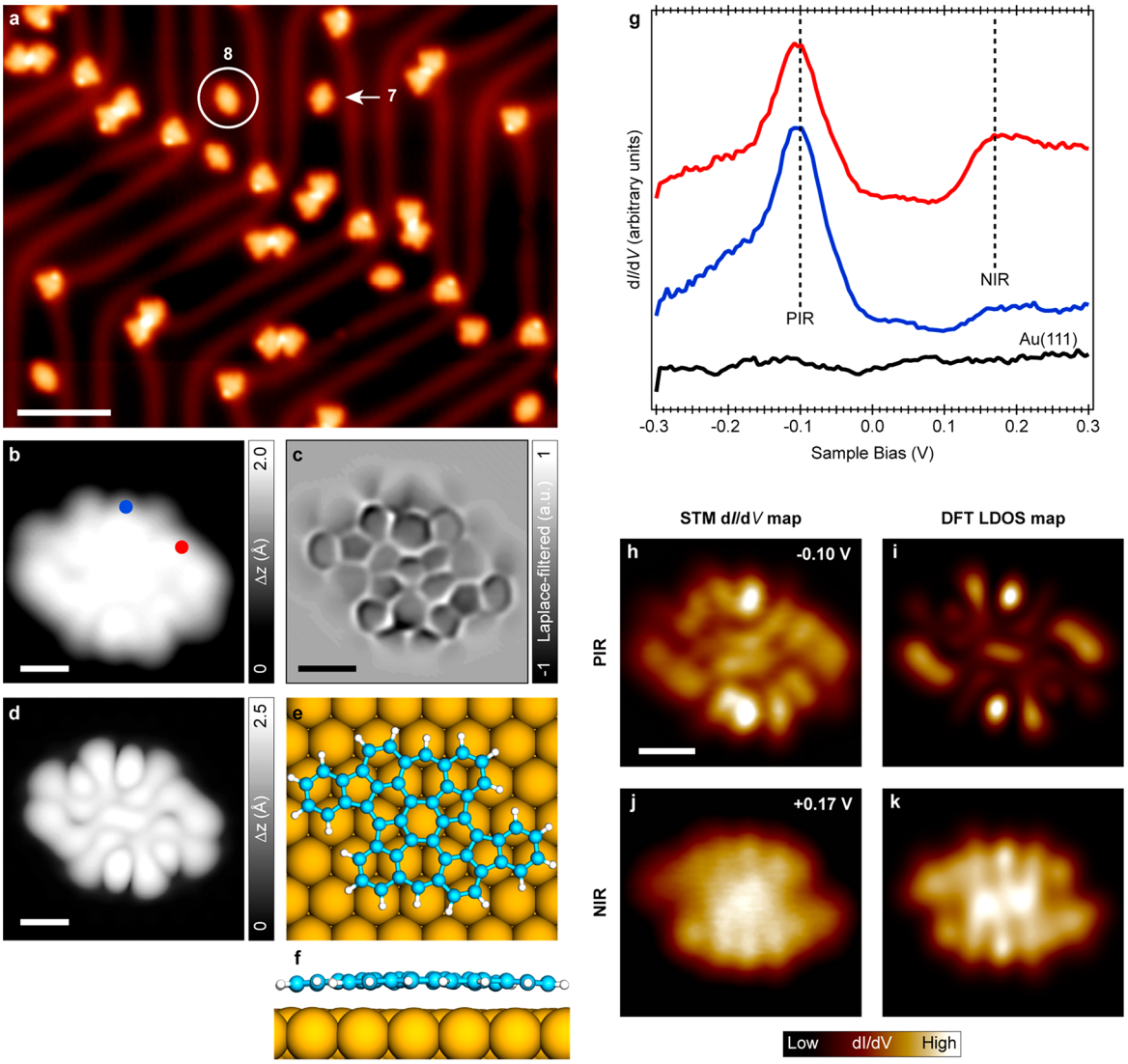

Figure 5. Structural and electronic characterization of the azulene-embedded nanographene **8** on Au(111). (a) Overview STM topography image of the surface after annealing to 250 °C (V = −1.00 V, I = 50 pA; scale bar 8 nm). The planar nanographene **8** is highlighted by a circle. Nanographene **7** containing unconjugated heptagonal rings is marked with an arrow. (b) High-resolution STM image of **8** acquired with a CO-functionalized tip (V = −0.12 V, I = 50 pA; scale bar 0.5 nm). (c) Corresponding Laplace-filtered UHR-STM image of **8** showing the chemical structure (open feedback parameters: V = −5 mV, I = 50 pA; Δz = −0.8 Å; scale bar 0.5 nm). (d) DFT-simulated STM image of 8 on Au(111) (V = −0.50 V; scale bar 0.5 nm). (e, f) Top and side views of the DFT-optimized equilibrium geometry of **8** on Au(111). (g) dI/dV spectra on **8** (tip positions marked with colored dots in panel b) acquired with a CO-functionalized tip, showing peaks in the DOS at −0.10 and +0.17 V corresponding to the PIR and the NIR, respectively. Reference spectrum on Au(111) is shown in black. The spectra are vertically shifted for clarity. (h, j) Experimental constant-height dI/dV maps of **8** acquired at the energies of the PIR and the NIR with a CO-functionalized tip. (i, k) DFT-simulated LDOS maps of the HOMO and the LUMO of **8**. Open feedback parameters for the dI/dV spectra: V = −0.30 V, I = 250 pA; V_{rms} = 12 mV. Open feedback parameters for the dI/dV maps: (h) V = −0.10 V, I = 150 pA, and (j) V = 0.17 V, I = 200 pA; V_{rms} = 12 mV. The scale bar of 0.5 nm in panel h also applies to panels i–k.

on **5** yield a large HOMO–LUMO gap of 2.70 eV on Au(111) (Figure S10), a value consistent with the conjugated core of 5,14-diaryldibenzo[*a*,*m*]rubicene,[42] thereby confirming the presence of unconjugated heptagonal rings. Figure 4d shows a high-resolution STM image of a square-shaped unit, where the noticeable features correspond to eight peripheral lobes that exhibit a weak contrast (apparent height = 2.1 Å), and four inner lobes of 3.7 Å in apparent height that exhibit a strong contrast. A careful comparison with the STM image of **5** establishes that these square-shaped units are self-assembled tetramers, wherein each constituent unit of the tetramer, **6**, results from the loss of one xylenyl group from **3b**, and the single xylenyl group present in the molecule manifests as the inner lobe exhibiting the strong contrast in STM images (Figure 1c, also see Figures S11, S12 for STM manipulation of the tetramers, and Figure S13 for a discussion regarding the loss of xylenyl groups). Finally, we address the structure of the self-assembled islands. Figure 4e shows a high-resolution STM image of an island. A closer inspection of the periphery of the island clearly establishes **6** as the constituent unit (a single unit of **6** is marked with an arrow in Figure 4e). Moreover, the orientation of **6** in each row is the same (a single row of molecules is highlighted with a red dashed line in Figure 4e), and is rotated by 180° in the adjacent row.

Having identified the species present on the surface, we annealed the sample to 250 °C to explore the possibility of

DOI: 10.1021/jacs.9b04718
J. Am. Chem. Soc. 2019, 141, 12011–12020

realizing fully conjugated nanographenes with embedded azulene units. As shown in Figure 5a, a range of products resulting from varying degrees of (cyclo)dehydrogenation reactions of **3b**, **5**, and **6** are present. In particular, we find two molecular species in minor quantities which exhibit an apparent planar topography (highlighted in Figure 5a), referred to as **7** (3% of 161 molecules) and **8** (13% of 161 molecules), and they are found adsorbed on the fcc regions of the surface. We target these two species for further characterization. As will be demonstrated, molecules **7** and **8** result from cyclodehydrogenative ring closure of the external phenyl groups of **5** and **6** to form two pentagonal rings (Figure 1c), with the heptagonal rings devoid of xylenyl groups. In **7** the apical carbon atoms of the heptagonal rings are bound to two hydrogen atoms, leading to a large HOMO−LUMO gap of 2.55 eV on Au(111)—about 0.15 eV smaller than **5** as a result of the extension of conjugation in **7** (see Figure S14 for the detailed structural and electronic characterizations). Compound **8**, as is detailed in the following discussion, corresponds to the case wherein the apical carbon atoms of the heptagonal rings underwent partial dehydrogenation to form a fully conjugated aromatic core (Figure 1c). Figure 5b shows a high-resolution STM image of **8** acquired with a CO-functionalized tip, wherein the molecule exhibits rich features in the LDOS at the chosen bias (i.e., −0.12 V). The structure of **8** is unambiguously confirmed via UHR-STM imaging (Figure 5c, also see Figure S15 for height-dependent UHR-STM imaging of **8**), which reveals the embedded azulene units at the core of the molecule. Cyclopenta fusion of the external phenyl groups to generate two new pentagonal rings is also evident in the image. Interestingly, the UHR-STM image demonstrates significant convolution of structural features with the LDOS particularly noticeable at the apexes of the heptagonal rings (see Figure S15). Since we did not observe such features in the UHR-STM images of **5** and **7** (Figure 4c and Figure S14) that consist of unconjugated heptagonal rings, it is plausible that annealing at this temperature has resulted in the loss of one hydrogen atom each from the apical sp^3 carbon atoms of the heptagonal rings, leading to the formation of fully conjugated rings. The simulated STM image (Figure 5d) of the DFT-optimized structure shown in Figure 5e,f exhibits remarkable agreement with the experimental STM image, thus confirming our speculation regarding the identity of **8**. The planar conformation of the molecule on the surface, evident in the UHR-STM image, is further confirmed by DFT calculations.

We performed STS measurements on **8** to probe its detailed electronic structure. Voltage-dependent differential conductance spectra (dI/dV vs V) acquired on **8** with a CO-functionalized tip (Figure 5g) shows a strong peak at −0.10 V and a shoulder at +0.17 V, against a featureless reference spectrum acquired over the bare Au(111) surface. We assign these peaks to the positive and the negative ion resonances (PIR and NIR) deriving from resonant tunneling of electrons through the HOMO and LUMO of **8**, respectively. Thus, the extracted HOMO−LUMO gap of **8** on Au(111) amounts to a remarkably low value of 0.27 eV, a substantial decrease of almost 90% compared to the gap of **7** as a result of the formation of fully conjugated heptagonal rings. Constant-height dI/dV maps acquired at the energies of the PIR and the NIR reveal significant intensities at the heptagonal rings (Figure 5h,j). Furthermore, DFT-calculated LDOS maps of the HOMO and the LUMO of **8** on Au(111) (Figure 5i,k), evaluated at a height of 5 Å above the molecular plane for a realistic comparison to the experimental conditions, show a remarkable agreement with the experimental dI/dV maps. We thus conclude that the features in the experimental dI/dV maps correspond to the spatial distribution of the probability densities of the HOMO and the LUMO wave functions of **8**. We further note that the regular appearance of dI/dV maps at both bias polarities strongly indicates the absence of any nonuniform interactions of **8** with the underlying surface. Furthermore, to clarify the effect of cyclopenta fusion on the change in electronic properties, we performed spin-polarized DFT calculations on **4a** and **8** (see Figure S16). We notice a change in the orbital distributions and a slight decrease of 0.18 eV of the HOMO−LUMO gap of **8** compared to **4a**, indicating that the electronic properties are not drastically affected with cyclopenta fusion.

Theoretical Characterization of the Electronic Ground State of 8. To theoretically assess the open-shell character of **8**, we calculated the occupation numbers of the UHF natural orbitals (NOs) of **8**. Our results reveal very high occupation numbers of the highest occupied and the lowest unoccupied NOs (HONO and LUNO), i.e., n_{HONO} = 1.04 and n_{LUNO} = 0.96 (Figure 6a). Based on the occupation numbers of the frontier NOs, the biradical index of **8** was calculated to be y_0 = 0.92 (see Methods for details), correlating with a large open-shell biradical character. Furthermore, the UHF-calculated electronic ground state of **8** converges to an open-shell singlet state, which is 0.45 eV lower than the open-shell triplet state. The UHF-calculated spin density distribution of **8** is

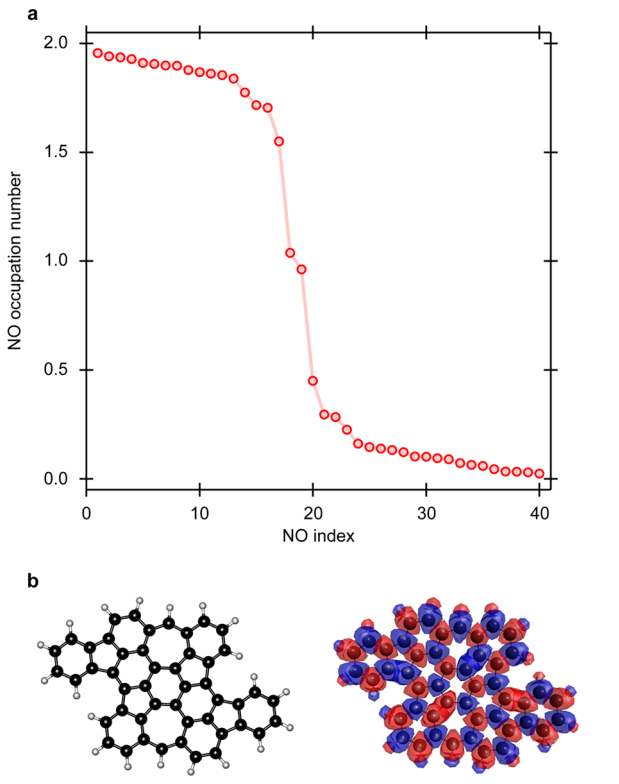

Figure 6. UHF calculations on **8**. (a) Evolution of the UHF-calculated natural orbital occupation numbers of **8** (filled circles). The frontier natural orbitals have large occupation numbers of n_{HONO} = 1.04 and n_{LUNO} = 0.96, leading to a pronounced biradical character in **8**. (b) DFT-optimized geometry (left) and UHF-calculated spin density distribution (right) of **8** (spin up, blue; spin down, red).

DOI: 10.1021/jacs.9b04718
J. Am. Chem. Soc. 2019, 141, 12011−12020

shown in Figure 6b. To verify the picture that emerges from our UHF calculations, we further performed higher level ab initio multiconfigurational computations for **8**. The GMC-QDPT2 computed ground state remains the open-shell singlet, separated from the open-shell triplet states with $S_z = 0$ and $S_z = 1$ by 0.12 and 0.54 eV, respectively. The closed-shell state lies much higher in energy at 0.95 eV. This confirms the distinct open-shell character of **8**.

DISCUSSION AND CONCLUSION

In summary, we explored the bottom-up synthesis of open-shell nanographenes with nonbenzenoid ring topologies both in solution and on a Au(111) surface. The resultant nanographene **4a** containing two pairs of embedded pentagonal and heptagonal rings was comprehensively studied in solution via a range of spectroscopic techniques (i.e., MALDI-TOF, NMR, EPR, and SQUID), which revealed a low optical gap (E_g^{opt} = 1.13 eV) and an open-shell singlet ground state with a low singlet−triplet gap (ΔE_{S-T} = −2.15 kcal/mol). Complementary STM studies of a cyclopenta-fused derivate **8** with submolecular resolution was conducted on a Au(111) surface, which unambiguously confirmed the chemical structure and revealed a low HOMO−LUMO gap of 0.27 eV. Insights into the open-shell character of **8** were provided via Hartree−Fock and multiconfigurational quantum chemical calculations, which confirm **8** to be a singlet biradicaloid with a pronounced open-shell biradical character (y_0 = 0.92). The nanographenes reported herein serve as model cases toward rational introduction of nonbenzenoid ring topologies, which could pave the way to tailor the local electronic and magnetic structures of carbon-based nanostructures. As an outlook, we propose to incorporate similar nonbenzenoid topologies into extended graphene nanostructures of technological interest, in particular in graphene nanoribbons, where the sensitive dependence of the intrinsic electronic properties on the edge and the π-bond topology allows for the engineering of novel functionalities.

METHODS

Synthesis. See the Supporting Information for detailed synthetic procedures for the compounds reported in this article. For NMR spectra of the compounds, see Figures S18−S57. For the crystal structure of compound **15a**, see Figure S58. For MALDI-TOF and ESI spectra of the compounds, see Figures S59−S71. The X-ray crystallographic coordinates for the structure reported in this article have been deposited at the Cambridge Crystallographic Data Centre (CCDC), under deposition number CCDC 1867280 (compound **15a**). The data can be obtained free of charge from the CCDC via the Web site http://www.ccdc.cam.ac.uk/data_request/cif.

Sample Preparation and STM Measurements. STM measurements were performed with a commercial low-temperature STM from Scienta Omicron operating at 5 K and base pressures below 1×10^{-10} mbar. Au(111) single crystal surface was prepared via multiple cycles of sputtering with Ar^+ ions at a pressure of $p = 6 \times 10^{-6}$ mbar, and annealing at 750 K for 10 min at $p < 1 \times 10^{-9}$ mbar. Precursor molecule **3b** was sublimed at 600 K on Au(111) surface held at room temperature, with $p \leq 2 \times 10^{-9}$ mbar during the course of sublimation. All STM images were acquired in constant-current mode unless otherwise noted. Indicated tunneling bias voltages are given with respect to the sample. Gold-coated tungsten tips were used for STM imaging and spectroscopy. dI/dV spectra and maps were acquired in constant-height mode using the lock-in technique (f = 860 Hz) to obtain a signal proportional to dI/dV from the first harmonic of the tunneling current. UHR-STM images were acquired in constant-height mode with a CO-functionalized tip, and the current signal was recorded. Open feedback parameters and subsequent approach distances (i.e., Δz) are provided in the respective figure captions. All STM images and dI/dV maps were processed with WSxM software.[43]

Theoretical Methods. To obtain the equilibrium geometries of the molecules adsorbed on the Au(111) substrate and to compute the corresponding STM images, we used the CP2K code[44,45] implementing DFT within a mixed Gaussian plane wave approach.[46] The surface/adsorbate systems were modeled within the repeated slab scheme;[47] i.e., a simulation cell contained four atomic layers of Au along the [111] direction and a layer of hydrogen atoms to passivate one side of the slab in order to suppress one of the two Au(111) surface states. A 40 Å of vacuum was included in the simulation cell to decouple the system from its periodic replicas in the direction perpendicular to the surface. The electronic states were expanded with a TZV2P Gaussian basis set[48] for C and H species and a DZVP basis set for Au species. A cutoff of 600 Ry was used for the plane wave basis set. Norm-conserving Goedecker−Teter−Hutter[49] pseudopotentials were used to represent the frozen core electrons of the atoms. We used the PBE parametrization for the generalized gradient approximation of the exchange−correlation functional.[50] We used the scheme proposed by Grimme to account for the van der Waals interactions.[51] We considered supercells of 41.64 × 41.21 Å corresponding to 224 surface units. To obtain the equilibrium geometries, we kept the atomic positions of the bottom two layers of the slab fixed to the ideal bulk positions, and all other atoms were relaxed until forces were lower than 0.005 eV/Å. To obtain simulated STM images[52,53] within the Tersoff−Hamann approximation,[54,55] we extrapolated the electronic orbitals to the vacuum region in order to correct the wrong decay in vacuum of the charge density due to the localized basis set.[55] Multiconfigurational self-consistent field (MC-SCF) and general multiconfiguration quasi-degenerate perturbation theory (GMC-QDPT2) computations based on occupationally restricted multiactive space configuration interaction (ORMAS-CI) were performed using the software GAMESS-US using a DZV basis set.[56] Both the triplet and the singlet states of the considered molecules were treated within a spin unrestricted formalism. UHF natural orbitals (NOs) were computed and used both to derive the biradical index defined as[57]

$$y_0 = 1 - \frac{2T}{1 + T^2}$$

with

$$T = \frac{n_{HONO} - n_{LUNO}}{2}$$

and as a starting point for the selection of the MC-SCF active space.[58] The active space used in MC-SCF and GMC-QDPT2 computations included 30 electrons in 30 orbitals divided in three subspaces [26−28/14; 0−4/2; 0−2/14] with a maximum allowed excitation of two electrons.

ASSOCIATED CONTENT

Supporting Information

The Supporting Information is available free of charge on the ACS Publications website at DOI: 10.1021/jacs.9b04718.

X-ray crystallographic coordinates of **15a** (CIF)

VT-^{1}H-NMR experiments of **4a**; EPR measurements; time-dependent UV−vis−NIR spectra and CV of **4a**; pristine precursor molecule (**3b**) on surface; STS of **5**; STM lateral and voltage-pulse-induced manipulation of self-assembled tetramers of **6**; loss of xylenyl groups from **3b**; structural and electronic characterization of **7** on Au(111); height-dependent UHR-STM images of **8**; spin-polarized DFT calculations on **4a** and **8**; synthetic procedures; NMR characterization; crystal structure of **15a**; MALDI-TOF and ESI spectra (PDF)

DOI: 10.1021/jacs.9b04718
J. Am. Chem. Soc. 2019, 141, 12011−12020

AUTHOR INFORMATION

Corresponding Authors

*muellen@mpip-mainz.mpg.de
*roman.fasel@empa.ch
*xinliang.feng@tu-dresden.de

ORCID

Junzhi Liu: 0000-0001-7146-0942
Shantanu Mishra: 0000-0002-2900-4203
Carlo A. Pignedoli: 0000-0002-8273-6390
José I. Urgel: 0000-0001-7608-2979
Alberto Fabrizio: 0000-0002-4440-3149
Hartmut Komber: 0000-0001-6176-6737
Clémence Corminboeuf: 0000-0001-7993-2879
Reinhard Berger: 0000-0002-8959-7821
Pascal Ruffieux: 0000-0001-5729-5354
Klaus Müllen: 0000-0001-6630-8786
Roman Fasel: 0000-0002-1553-6487
Xinliang Feng: 0000-0003-3885-2703

Author Contributions

○J.L. and S.M. contributed equally to this work.

Notes

The authors declare no competing financial interest.

ACKNOWLEDGMENTS

This work was financially supported by European Union's Horizon 2020 research and innovation program under Grant Agreement No. 696656 (Graphene Flagship Core2), the German Research Foundation (DFG) within the Cluster of Excellence "Center for Advancing Electronics Dresden (cfaed)" and EnhanceNano (No. 391979941), the European Social Fund and the Federal State of Saxony (ESF-Project "GRAPHD", TU Dresden), the Swiss National Science Foundation, and the NCCR MARVEL funded by the Swiss National Science Foundation. Calculations were supported by a grant from the Swiss National Supercomputing Centre (CSCS) under project ID s746. We thank Dr. Dieter Schollmeyer (Institute for Organic Chemistry, Johannes Gutenberg University Mainz) for single-crystal X-ray structural analysis and Mr. Chi Xu (Helmholtz-Zentrum Dresden-Rossendorf, Institute of Ion Beam Physics and Materials Research) for the SQUID measurement.

REFERENCES

(1) Wu, J.; Pisula, W.; Müllen, K. Graphenes as potential material for electronics. *Chem. Rev.* **2007**, *107*, 718−747.
(2) Chen, L.; Hernandez, Y.; Feng, X.; Müllen, K. From nanographene and graphene nanoribbons to graphene sheets: chemical synthesis. *Angew. Chem., Int. Ed.* **2012**, *51*, 7640−7654.
(3) Narita, A.; Wang, X. Y.; Feng, X.; Müllen, K. New advances in nanographene chemistry. *Chem. Soc. Rev.* **2015**, *44*, 6616−6643.
(4) Wang, X. Y.; Narita, A.; Müllen, K. Precision synthesis versus bulk-scale fabrication of graphenes. *Nat. Rev. Chem.* **2017**, *2*, No. 0100.
(5) Clar, E.; John, F. Polynuclear aromatic hydrocarbons and their derivatives. V.Naphthoanthracenes, their oxidation products and a new class of deeply colored hydrocarbons. *Ber. Dtsch. Chem. Ges. B* **1929**, *62*, 3021−3029.
(6) Clar, E.; Ironside, C. T.; Zander, M. The electronic interaction between benzenoid rings in condensed aromatic hydrocarbons. 1:12−2:3−4:5−6:7−8:9−10: ll-hexabenzocoronene, 1:2−3:4−5:6−10:11-tetrabenzoanthanthrene, and 4:5−6:7−11:12−13:14-tetrabenzoperopyrene. *J. Chem. Soc.* **1959**, 142−147.
(7) Scholl, R.; Seer, C.; Weitzenböck, R. Perylen, ein hoch kondensierter aromatischer Kohlenwasserstoff $C_{20}H_{12}$. *Ber. Dtsch. Chem. Ges.* **1910**, *43*, 2202−2209.
(8) Cai, J.; Ruffieux, P.; Jaafar, R.; Bieri, M.; Braun, T.; Blankenburg, S.; Muoth, M.; Seitsonen, A. P.; Saleh, M.; Feng, X.; Müllen, K.; Fasel, R. Atomically precise bottom-up fabrication of graphene nanoribbons. *Nature* **2010**, *466*, 470−473.
(9) Narita, A.; Feng, X.; Hernandez, Y.; Jensen, S. A.; Bonn, M.; Yang, H.; Verzhbitskiy, I. A.; Casiraghi, C.; Hansen, M. R.; Koch, A. H. R.; Fytas, G.; Ivasenko, O.; Li, B.; Mali, K. S.; Balandina, T.; Mahesh, S.; De Feyter, S.; Müllen, K. Synthesis of structurally well-defined and liquid-phase-processable graphene nanoribbons. *Nat. Chem.* **2014**, *6*, 126−132.
(10) Chen, Y. C.; Cao, T.; Chen, C.; Pedramrazi, Z.; Haberer, D.; de Oteyza, D. G.; Fischer, F. R.; Louie, S. G.; Crommie, M. F. Molecular bandgap engineering of bottom-up synthesized graphene nanoribbon heterojunctions. *Nat. Nanotechnol.* **2015**, *10*, 156−160.
(11) Liu, J.; Li, B. W.; Tan, Y. Z.; Giannakopoulos, A.; Sanchez-Sanchez, C.; Ruffieux, P.; Beljonne, D.; Fasel, R.; Feng, X.; Müllen, K. Toward cove-edged low band gap graphene nanoribbons. *J. Am. Chem. Soc.* **2015**, *137*, 6097−6103.
(12) Ruffieux, P.; Wang, S.; Yang, B.; Sanchez-Sanchez, C.; Liu, J.; Dienel, T.; Talirz, L.; Shinde, P.; Pignedoli, C. A.; Passerone, D.; Dumslaff, T.; Feng, X.; Muellen, K.; Fasel, R. On-surface synthesis of graphene nanoribbons with zigzag edge topology. *Nature* **2016**, *531*, 489−492.
(13) Yang, W.; Lucotti, A.; Tommasini, M.; Chalifoux, W. A. Bottom-up synthesis of soluble and narrow graphene nanoribbons using alkyne benzannulations. *J. Am. Chem. Soc.* **2016**, *138*, 9137−9144.
(14) Gao, J.; Uribe-Romo, F. J.; Saathoff, J. D.; Arslan, H.; Crick, C. R.; Hein, S. J.; Itin, B.; Clancy, P.; Dichtel, W. R.; Loo, Y. L. Ambipolar transport in solution-synthesized graphene nanoribbons. *ACS Nano* **2016**, *10*, 4847−4856.
(15) Byers, P. M.; Alabugin, I. V. Polyaromatic ribbons from oligo-alkynes via selective radical cascade: stitching aromatic rings with polyacetylene bridges. *J. Am. Chem. Soc.* **2012**, *134*, 9609−9614.
(16) Ball, M.; Zhong, Y.; Wu, Y.; Schenck, C.; Ng, F.; Steigerwald, M.; Xiao, S.; Nuckolls, C. Contorted polycyclic aromatics. *Acc. Chem. Res.* **2015**, *48*, 267−276.
(17) Frederickson, C. K.; Rose, B. D.; Haley, M. M. Explorations of the indenofluorenes and expanded quinoidal analogues. *Acc. Chem. Res.* **2017**, *50*, 977−987.
(18) Scott, L. T.; Jackson, E. Q.; Zhang, Q.; Steinberg, B. D.; Bancu, M.; Li, B. A Short, Rigid, structurally pure carbon nanotube by stepwise chemical synthesis. *J. Am. Chem. Soc.* **2012**, *134*, 107−110.
(19) Eliseeva, M. N.; Scott, L. T. Pushing the Ir-catalyzed C−H polyborylation of aromatic compounds to maximum capacity by exploiting reversibility. *J. Am. Chem. Soc.* **2012**, *134*, 15169−15172.
(20) Bheemireddy, S. R.; Ubaldo, P. C.; Rose, P. W.; Finke, A. D.; Zhuang, J.; Wang, L.; Plunkett, K. N. Stabilizing pentacene by cyclopentannulation. *Angew. Chem., Int. Ed.* **2015**, *54*, 15762−15766.
(21) Pun, S. H.; Miao, Q. Toward negatively curved carbons. *Acc. Chem. Res.* **2018**, *51*, 1630−1642.
(22) Banhart, F.; Kotakoski, J.; Krasheninnikov, A. V. Structural defects in graphene. *ACS Nano* **2011**, *5*, 26−41.
(23) Huang, P. Y.; Ruiz-Vargas, C. S.; van der Zande, A. M.; Whitney, W. S.; Levendorf, M. P.; Kevek, J. W.; Garg, S.; Alden, J. S.; Hustedt, C. J.; Zhu, Y.; Park, J.; McEuen, P. L.; Muller, D. A. Grains and grain boundaries in single-layer graphene atomic patchwork quilts. *Nature* **2011**, *469*, 389−392.
(24) Kawasumi, K.; Zhang, Q.; Segawa, Y.; Scott, L. T.; Itami, K. A grossly warped nanographene and the consequences of multiple odd-membered-ring defects. *Nat. Chem.* **2013**, *5*, 739−744.
(25) Cheung, K. Y.; Xu, X.; Miao, Q. Aromatic saddles containing two heptagons. *J. Am. Chem. Soc.* **2015**, *137*, 3910−3914.
(26) Rasool, H. I.; Ophus, C.; Zettl, A. A. Atomic defects in two dimensional materials. *Adv. Mater.* **2015**, *27*, 5771−5777.

DOI: 10.1021/jacs.9b04718
J. Am. Chem. Soc. 2019, 141, 12011−12020

(27) Hieulle, J.; Carbonell-Sanromà, E.; Vilas-Varela, M.; Garcia-Lekue, A.; Guitián, E.; Peña, D.; Pascual, J. I. On-surface route for producing planar nanographenes with azulene moieties. *Nano Lett.* **2018**, *18*, 418−423.
(28) Tobe, Y. Non-alternant non-benzenoid aromatic compounds: past, present, and future. *Chem. Rec.* **2015**, *15*, 86−96.
(29) Miyoshi, H.; Nobusue, S.; Shimizu, A.; Tobe, Y. Non-alternant non-benzenoid kekulenes: the birth of a new kekulene family. *Chem. Soc. Rev.* **2015**, *44*, 6560−6577.
(30) Müllen, K. Molecular defects in organic materials. *Nat. Rev. Mater.* **2016**, *1*, 15013.
(31) Hu, P.; Wu, J. Modern zethrene chemistry. *Can. J. Chem.* **2017**, *95*, 223−233.
(32) Konishi, A.; Kubo, K. Benzenoid quinodimethanes. *Top Curr. Chem.* **2017**, *375*, 83.
(33) Ajayakumar, M. R.; Fu, Y.; Ma, J.; Hennersdorf, F.; Komber, H.; Weigand, J. J.; Alfonsov, A.; Popov, A. A.; Berger, R.; Liu, J.; Müllen, K.; Feng, F. Toward full zigzag-edged nanographenes: peritetracene and its corresponding circumanthracene. *J. Am. Chem. Soc.* **2018**, *140*, 6240−6244.
(34) Datta, S.; Cai, Y.; Yudhistira, I.; Zeng, Z.; Zhang, Y.; Zhang, H.; Adam, S.; Wu, J.; Loh, K. P. Tuning magnetoresistance in molybdenum disulphide and graphene using a molecular spin transition. *Nat. Commun.* **2017**, *8*, 677.
(35) Zeng, Z.; Shi, X.; Chi, C.; Lopez Navarrete, J. T.; Casado, J.; Wu, J. Pro-aromatic and anti-aromatic p-conjugated molecules: an irresistible wish to be diradicals. *Chem. Soc. Rev.* **2015**, *44*, 6578−6596.
(36) Liu, C.; Sandoval-Salinas, M. E.; Hong, Y.; Gopalakrishna, T. Y.; Phan, H.; Aratani, N.; Herng, T. S.; Ding, J.; Yamada, H.; Kim, D.; Casanova, D.; Wu, J. Macrocyclic polyradicaloids with unusual super-ring structure and global aromaticity. *Chem.* **2018**, *4*, 1586−1595.
(37) Mishra, S.; Lohr, T. G.; Pignedoli, C. A.; Liu, J.; Berger, R.; Urgel, J. I.; Müllen, K.; Feng, F.; Ruffieux, P.; Fasel, R. Tailoring bond topologies in open-Shell graphene nanostructures. *ACS Nano* **2018**, *12*, 11917−11927.
(38) Yamamoto, K.; Ie, Y.; Tohnai, N.; Kakiuchi, F.; Aso, Y. Antiaromatic character of cycloheptatriene-bis-annelated indenofluorene framework mainly originated from heptafulvene segment. *Sci. Rep.* **2018**, *8*, 17663.
(39) Sun, Z.; Zeng, Z.; Wu, J. Zethrenes, extended *p*-quinodimethanes, and periacenes with a singlet biradical ground state. *Acc. Chem. Res.* **2014**, *47*, 2582−2591.
(40) Weiss, C.; Wagner, C.; Kleimann, C.; Rohlfing, M.; Tautz, F. S.; Temirov, R. Imaging Pauli repulsion in scanning tunneling microscopy. *Phys. Rev. Lett.* **2010**, *105*, No. 086103.
(41) Kichin, G.; Weiss, C.; Wagner, C.; Tautz, F. S.; Temirov, R. Single molecule and single atom sensors for atomic resolution imaging of chemically complex surfaces. *J. Am. Chem. Soc.* **2011**, *133*, 16847−16851.
(42) Liu, J.; Narita, A.; Osella, S.; Zhang, W.; Schollmeyer, D.; Beljonne, D.; Feng, X.; Müllen, K. Unexpected Scholl reaction of 6,7,13,14-tetraarylbenzo[*k*]tetraphene: selective formation of five-membered rings in polycyclic aromatic hydrocarbons. *J. Am. Chem. Soc.* **2016**, *138*, 2602−2608.
(43) Horcas, I.; Fernández, R.; Gómez-Rodríguez, J. M.; Colchero, J.; Gómez-Herrero, J.; Baro, A. M. WSXM: a software for scanning probe microscopy and a tool for nanotechnology. *Rev. Sci. Instrum.* **2007**, *78*, No. 013705.
(44) The CP2K developers group. Available at http://www.cp2k.org.
(45) Hutter, J.; Iannuzzi, M.; Schiffmann, F.; VandeVondele, J. cp2k: atomistic simulations of condensed matter systems. *Wiley Interdiscip. Rev. Comput. Mol. Sci.* **2014**, *4*, 15−25.
(46) VandeVondele, J.; Krack, M.; Mohamed, F.; Parrinello, M.; Chassaing, T.; Hutter, J. Quickstep: Fast and accurate density functional calculations using a mixed Gaussian and plane waves approach. *Comput. Phys. Commun.* **2005**, *167*, 103−128.
(47) Pickett, W. E. Pseudopotential methods in condensed matter applications. *Comput. Phys. Rep.* **1989**, *9*, 115−197.
(48) VandeVondele, J.; Hutter, J. Gaussian basis sets for accurate calculations on molecular systems in gas and condensed phases. *J. Chem. Phys.* **2007**, *127*, 114105.
(49) Goedecker, S.; Teter, M.; Hutter, J. Separable dual-space Gaussian pseudopotentials. *Phys. Rev. B: Condens. Matter Mater. Phys.* **1996**, *54*, 1703−1710.
(50) Perdew, J. P.; Burke, K.; Ernzerhof, M. Generalized gradient approximation made simple. *Phys. Rev. Lett.* **1996**, *77*, 3865−3868.
(51) Grimme, S.; Antony, J.; Ehrlich, S.; Krieg, H. A consistent and accurate ab initio parametrization of density functional dispersion correction (DFT-D) for the 94 elements H-Pu. *J. Chem. Phys.* **2010**, *132*, 154104.
(52) Gaspari, R.; Blankenburg, S.; Pignedoli, C. A.; Ruffieux, P.; Treier, M.; Fasel, R.; Passerone, D. s-orbital continuum model accounting for the tip shape in simulated scanning tunneling microscope images. *Phys. Rev. B: Condens. Matter Mater. Phys.* **2011**, *84*, 125417.
(53) Talirz, L. *Toolkit Using the Atomistic Simulation Environment (ASE)*; 2015. Available at https://github.com/ltalirz/asetk.
(54) Tersoff, J.; Hamann, D. R. Theory of the scanning tunneling microscope. *Phys. Rev. B: Condens. Matter Mater. Phys.* **1985**, *31*, 805−813.
(55) Tersoff, J. Method for the calculation of scanning tunneling microscope images and spectra. *Phys. Rev. B: Condens. Matter Mater. Phys.* **1989**, *40*, 11990−11993.
(56) Schmidt, M. W.; Baldridge, K. K.; Boatz, J. A.; Elbert, S. T.; Gordon, M. S.; Jensen, J. H.; Koseki, S.; Matsunaga, N.; Nguyen, K. A.; Su, S.; Windus, T. L.; Dupuis, M.; Montgomery, J. A. General atomic and molecular electronic structure system. *J. Comput. Chem.* **1993**, *14*, 1347−1363.
(57) Marković, S.; Djurdjevic, J.; Jeremic, S.; Gutman, I. Diradical character of some fluoranthenes. *J. Serb. Chem. Soc.* **2010**, *75*, 1241−1249.
(58) Pulay, P.; Hamilton, T. UHF natural orbitals for defining and starting MC-SCF calculations. *J. Chem. Phys.* **1988**, *88*, 4926−4933.

DOI: 10.1021/jacs.9b04718
J. Am. Chem. Soc. 2019, 141, 12011−12020